

Increasing the stability of a superfluid in a rotating necklace potential

Giulio Nesti¹ and Luca Pezzè^{1,2}

¹European Laboratory for Nonlinear Spectroscopy (LENS), University of Florence, 50019 Sesto Fiorentino, Italy

²Istituto Nazionale di Ottica del Consiglio Nazionale delle Ricerche (CNR-INO), Largo Enrico Fermi 6, 50125 Firenze, Italy

Recent experiments have probed the stability of ring superfluids in the presence of Josephson barriers or Gaussian impurities. Here we present a theoretical analysis that extends beyond the regimes explored so far. We study the onset of dynamical instabilities induced by a one-dimensional potential rotating at an effective angular velocity ω , addressing both the tunneling and the hydrodynamic regimes. We show that the critical angular velocity ω_c increases almost linearly with the number of barriers, with a slope set by their height and width. When the system is quenched into the dynamically unstable regime, it emits multiple solitons, which can switch or even reverse the direction of circulation. The stabilization mechanism is robust against imperfections of the potential and does not require a perfectly periodic array of barriers. In particular, we find that adding a disordered speckle potential to an ordered array of barriers can further increase ω_c : disorder can therefore make a ring superfluid more resilient to dynamical instabilities.

I. INTRODUCTION

Degenerate quantum gases are ideal clean platforms to study several fascinating aspects associated with the interplay of superfluidity and impurity-induced dissipation [1–7]. Early demonstrations of superfluidity in these systems [8–13, 23] have paved the way to recent quantification of the superfluid fraction [14, 15] in periodic potentials [16] and supersolids [17]. Controlled dissipation can be induced by external optical lattices [18, 19], disordered potentials [20–22], or Gaussian impurities [23–25].

A particularly interesting platform are ultracold gases in ring traps [26–28]. In absence of additional external potentials, ring superfluids can support current states with finite quantized circulation. This has been experimentally demonstrated in both bosonic [27, 29, 30] and fermionic [31, 32] ultracold gases, with persistent currents of multiple circulation quanta and lifetimes of the order of seconds. Ring traps can be further equipped with additional external potentials. Experiments with a single rotating barrier or weak link have investigated the onset of phase slips processes [37], hysteresis [33] and current–phase relation [34]. Superfluidity holds only up to a critical relative velocity between the fluid and the potential: above this threshold, excitations become energetically favorable and the flow becomes dissipative [35–40]. More recently, the experimental and theoretical attention has been devoted to the ring superfluids with several potential barriers. In Ref. [50, 51] a ring with two movable barriers have realized a superfluid analogue of SQUIDs. Reference [52] investigated the transport properties in a toroidal Bose–Einstein condensate (BEC) equipped with a controllable number, n , of tunneling barriers. It was shown that, in the tunneling regime ($V_0/\mu > 1$), the Josephson critical current J_c increases with n . A similar effect has been observed in further experiments with a toroidal BEC and a variable number of localized Gaussian impurities [53] of size comparable with the BEC healing length.

In this manuscript, we extend the characterization of necklace superfluids beyond the regime of parameters and phenomena studied so far [52, 53]. We consider a BEC in a one-dimensional (1D) ring equipped with n barriers that co-rotate

at an effective angular frequency ω . We address two different scenarios, see Fig.1. In the so-called *clean necklace*, Fig.1(a), the barriers are identical and periodically arranged. For effective rotation frequencies below a critical value, $\omega \leq \omega_c$, the system exhibits a stable ground state flow. For $\omega > \omega_c$, a dynamical instability is triggered when the local phase jump –

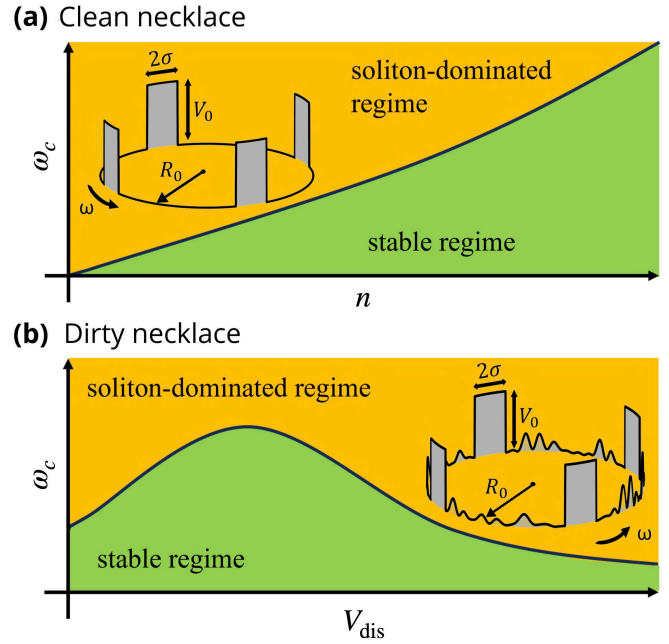


FIG. 1. Schematic summary of the main results of this work. Our system is a 1D ring BEC including potential barriers rotating at an effective frequency ω . We distinguish a regime where the BEC supports stationary (stable) solutions (green region) and a regime where the system becomes dynamically unstable due to soliton emission (yellow region). These are separated by a critical frequency ω_c (black line). (a) Clean necklace. The potential consists of n identical barriers of height V_0 and half-width σ (inset). We find that $\omega_c(n)$ increases monotonically with n , with a slope set by the interaction strength and the barrier height and width. (b) Dirty necklace. Here a disordered background potential of maximum amplitude V_{dis} is superposed to the clean necklace (inset). We find that ω_c increases further with V_{dis} , reaching a maximum for $V_{\text{dis}} \approx V_0$.

or, equivalently, the maximum superfluid velocity – exceeds a critical threshold. A square-barrier model provides analytical insights to the instability mechanism and yields an explicit expression for ω_c . A key result is that ω_c increases with the number of barriers n , as schematically indicated in Fig. 1(a). This enhanced stability is a consequence of circulation quantization in the ring: the phase drop across each barrier scales as $\delta\phi \sim 1/n$, thereby suppressing the onset of phase slips as n increases. Although a similar topological mechanism was previously identified in the scaling of the maximum sustainable current J_c in the clean necklace [52], we emphasize that J_c and ω_c characterize distinct properties of the system. In particular, the maximum current does not generally occur at $\omega = \omega_c$. We show that the increase of ω_c with n is robust over a wide range of interaction strengths and barrier parameters (height V_0 and width σ). This behavior persists in the hydrodynamic regime ($\xi \ll \sigma$, with ξ being the healing length), in the Josephson regime ($V_0/\mu > 1$, with μ being the chemical potential), and in the weak-link regime ($V_0/\mu \leq 1$, $\xi \geq \sigma$), while being insensitive to the detailed shape of the barriers. For quenches to $\omega > \omega_c$, we observe a soliton-dominated response in which n solitons – one per barrier – are generated simultaneously. By varying n , the resulting dynamics can reverse the initial circulation, enabling the realization of a superfluid switch or inverter. We also analyze a *dirty necklace* configuration, Fig. 1(b), in which a disordered potential is present between the barriers. We find that ω_c further increases with the height of the disordered potential, V_{dis} , relative to the barriers height. A resonant response occurs for $V_{\text{dis}} \approx V_0$ where the ω_c reaches a maximum. Thus, contrary to common-sense expectations, weak disorder enhances the stability of the necklace superfluid against dynamical instabilities. As in the clean case, quenches into the unstable regime allow for controlled inversion of the superfluid circulation and tailored vortex emission.

II. SUPERFLUID NECKLACE

The BEC is confined to a 1D ring of radius R and equipped with a repulsive potential $V(\theta)$, where θ is the azimuthal angle. Following Ref. [52], we refer to this configuration as a *superfluid necklace*. The explicit form of $V(\theta)$, specified below, distinguishes between clean and disordered (“dirty”) realizations. We investigate the stability of the BEC when the potential is rotated at angular velocity Ω with respect to the laboratory frame. In the co-rotating frame, the dimensionless Gross-Pitaevskii equation (GPE) reads

$$\left[-\frac{1}{2} \frac{\partial^2}{\partial \theta^2} + g|\Psi(\theta, t)|^2 + V(\theta) + i\Omega \frac{\partial}{\partial \theta} \right] \Psi(\theta, t) = i \frac{\partial}{\partial t} \Psi(\theta, t) \quad (1)$$

where g is the coupling constant and $\Psi(\theta, t)$ is the order parameter, normalized as $\int_0^{2\pi} |\Psi(\theta, t)|^2 d\theta = 1$. Energies, angular velocities and times are measured in units of $E_R \equiv \hbar^2/mR^2$, $\Omega_R \equiv \hbar/mR^2$ and $t_R \equiv mR^2/\hbar$, respectively, where m is the atomic mass. Due to the multiply connected geometry, the single-valuedness condition on the wavefunction imposes the

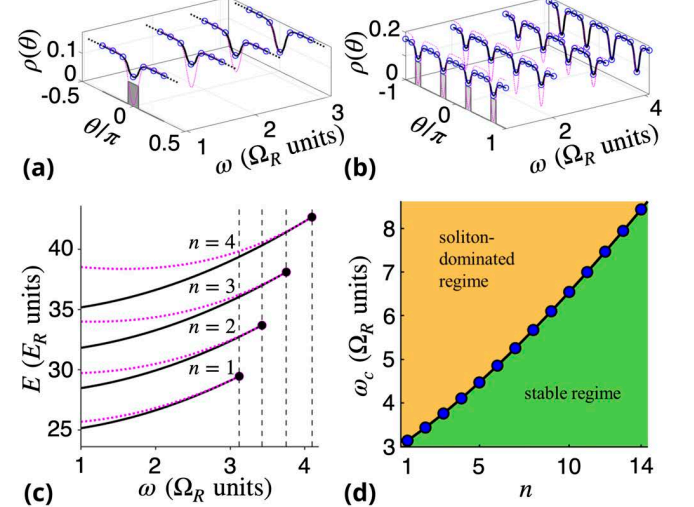


FIG. 2. Top panels show the analytical density profiles of the ground (solid black) and excited (dotted pink) states, Eqs. (10) and (11), for $n = 1$ (a) and $n = 4$ (b), respectively. The density is plotted as a function of both the azimuthal angle θ and the effective rotation frequency ω . Blue dots indicate the numerical ground-state density obtained by solving Eq. (8). The gray shaded areas represent the external potential of Eq. (9). Panel (c) displays the mean-field energy, Eq. (12), of the ground (solid black) and excited (dotted pink) states as a function of ω . Different curves correspond to different values of n and are vertically offset for clarity. Vertical lines and filled dots highlight the critical frequency ω_c . Panel (d) shows $\omega_c(n)$ as a function of the number of barriers n (blue dots); the solid line is a guide to the eye. Green (yellow) shading indicates the stable (unstable) region, as in Fig. 1(a). In all panels, the parameters are $g = 300$, $V_0/\mu \approx 0.4$, and $\sigma/\xi \approx 0.5$.

quantization condition

$$\int_0^{2\pi} v(\theta, t) d\theta = 2\pi v(t), \quad (2)$$

where $v(t)$ is an integer winding number, which may depend on time (see below), $v(\theta, t) = \partial_\theta \phi(\theta, t)$ is the superfluid angular velocity in units of $v_R = R\Omega_R = mR/\hbar$, and $\phi(\theta, t)$ is the condensate phase.

At equilibrium, the order parameter evolves in time through the chemical potential μ ,

$$\Psi(\theta, t) = \sqrt{\rho(\theta)} e^{i[\phi(\theta) - \mu t]}, \quad (3)$$

where $\rho(\theta)$ is the stationary density profile. With this ansatz, Eq. (1) separates into two equations [3]. The imaginary part yields a continuity equation, which defines the superfluid current

$$J = \rho(\theta) [v(\theta) - \Omega] \quad (4)$$

in the chosen dimensionless units. In the static case the current is spatially uniform along the ring, so that $\partial J/\partial\theta = 0$. Substituting Eq. (4) into Eq. (2) gives

$$J = \frac{\omega f_s}{2\pi}, \quad (5)$$

where

$$f_s = (2\pi)^2 \left(\int_0^{2\pi} \frac{d\theta}{\rho(\theta)} \right)^{-1} \quad (6)$$

is Leggett's superfluid fraction [14, 15, 52], and

$$\omega = \nu - \Omega \quad (7)$$

is the effective rotation frequency. The real part of Eq. (1) provides an equation for the density,

$$\mu_0 \sqrt{\rho(\theta)} = \left(-\frac{1}{2} \frac{\partial^2}{\partial \theta^2} + \frac{1}{2} \frac{J^2}{\rho(\theta)^2} + V(\theta) + g\rho(\theta) \right) \sqrt{\rho(\theta)}, \quad (8)$$

where $\mu_0 = \mu + \Omega^2/2$. Thus, the effect of rotation is fully absorbed into the current J , together with a shift of the chemical potential by $\Omega^2/2$, making Eq. (8) formally equivalent to the stationary GPE of a non-rotating condensate. The ground state of the system is obtained by solving Eqs. (4) and (8) self-consistently, via imaginary-time propagation, starting from a uniform initial wavefunction.

III. CLEAN NECKLACE

We define the clean superfluid necklace as the case of n identical barriers uniformly distributed along the ring. Throughout most of this work we consider square barriers, which allow for analytical solutions of the GPE (see below). The potential is then given by

$$V(\theta) = \begin{cases} V_0, & \text{for } \theta \in [\theta_j - \sigma, \theta_j + \sigma], \\ 0, & \text{otherwise,} \end{cases} \quad (9)$$

for $j = 1, \dots, n$, where n is the number of barriers, V_0 and σ are the height and half-width of each barrier, respectively, and $\theta_j = 2\pi j/n$ is the position of the j -th barrier. An example of the corresponding potential profile is shown in the inset of Fig. 1(a). Our main results are qualitatively insensitive to the detailed barrier shape; this point is discussed in the Appendix.

A. Analytical solutions of the GPE

To investigate the stability properties of the BEC, we rely on analytical solutions of Eq. (8). For a single static square barrier in an infinite 1D geometry, exact solutions are known in terms of Jacobi elliptic functions [54, 55]. In this case, the density profile inside the potential barrier takes the form

$$\rho_{\text{in}}(\theta) = \begin{cases} \rho_0 + \rho_1 \frac{s^2(\alpha_1 \theta, m_1)}{c^2(\alpha_1 \theta, m_1)}, & \text{if } \Delta \geq 0 \text{ and } \rho_1 \geq 0, \\ \rho_0 + \rho_2 \frac{1 - c(\alpha_2 \theta, m_2)}{1 + c(\alpha_2 \theta, m_2)}, & \text{otherwise,} \end{cases} \quad (10)$$

where $s(z, m)$ and $c(z, m)$ are Jacobi sine and cosine functions, with argument $z = \alpha_i \theta$ and elliptic modulus $k_i = \sqrt{m_i}$, and ρ_0 is the density at the center of the barrier. The density profile

outside the potential barrier, where the external potential (9) vanishes, is

$$\rho_{\text{out}}(\theta) = \frac{J^2}{g \rho_b^2} + c_b \tanh^2 \left(\sqrt{1 - \frac{2\xi_b^2 J^2}{\rho_b^2}} \frac{\theta - \sigma}{\sqrt{2} \xi_b} + \phi_0 \right)^2. \quad (11)$$

Here, ρ_b is the bulk density, $\xi_b = 1/\sqrt{2g\rho_b}$ is the bulk healing length; the coefficients entering Eqs. (10) and (11) are reported in Ref. [56]. As shown in Refs. [54, 55], Eqs. (10) and (11) admit two distinct, non-degenerate pairs of solutions, corresponding to two different values of ρ_0 . One solution corresponds to the lowest-energy configuration (ground state), while the other represents a higher-energy configuration (excited state). For the infinite system of Ref. [55], in the absence of a potential barrier the ground state reduces to a plane wave and the excited state to a dark soliton.

We use Eqs. (10) and (11) as approximate solutions for our 1D ring with n rotating barriers, provided that the angular distance between neighboring barriers, $\theta_{j+1} - \theta_j$, is much larger than both the bulk healing length ξ and the barrier width σ . Under this condition, a bulk region with constant density ρ_b can be defined. A key difference from the infinite 1D line considered in Refs. [54, 55] is that, in our toroidal geometry, the parameters ρ_b , J , and μ cannot be imposed externally: they must be determined self-consistently from the quantization condition Eq. (2) and, for finite ω , by numerically solving Eq. (8). A major advantage of the analytical approach is that it gives access to the excited state of the rotating system, which in turn provides information on the stability of the condensate at finite ω .

Figures 2(a) and 2(b) show the density profiles of the ground and excited states obtained for $n = 1$ and $n = 4$, respectively, as a function of ω . In both cases, the density reaches its minimum at the center of the barrier, where the external potential (indicated by gray shaded areas) suppresses the condensate density. The numerical ground-state solution (circles) is in excellent agreement with the analytical expression given by Eqs. (10) and (11) (black solid line). Inside the barrier, the excited state (pink line) attains a lower density than the ground state, reflecting a larger kinetic energy. As ω approaches a critical value ω_c , the two solutions merge. For $\omega > \omega_c$ no convergent numerical solution of the GPE is found. As confirmed below, by studying the evolution of the system following a small quench of ω , the critical value ω_c marks the onset of a dynamical instability, signaled by the spontaneous emission of solitons in the 1D system.

To further characterize the stability phenomenon, Fig. 2(c) displays the mean-field energy

$$E = \int_0^{2\pi} d\theta \left(-\frac{1}{2} \sqrt{\rho} \frac{\partial^2}{\partial \theta^2} \sqrt{\rho} + \sqrt{\rho} V \sqrt{\rho} + \frac{g}{2} \rho^2 + \frac{1}{2} \frac{J^2}{\rho} \right) \quad (12)$$

of the ground (solid lines) and excited (dashed lines) states as a function of the rotation frequency ω for different numbers of barriers n . At ω_c , the energy of the ground state becomes degenerate with that of the excited state, in analogy with bifurcation processes [47, 57, 58]. We emphasize that, according to Eq. (7), the effective critical frequency can be accessed by

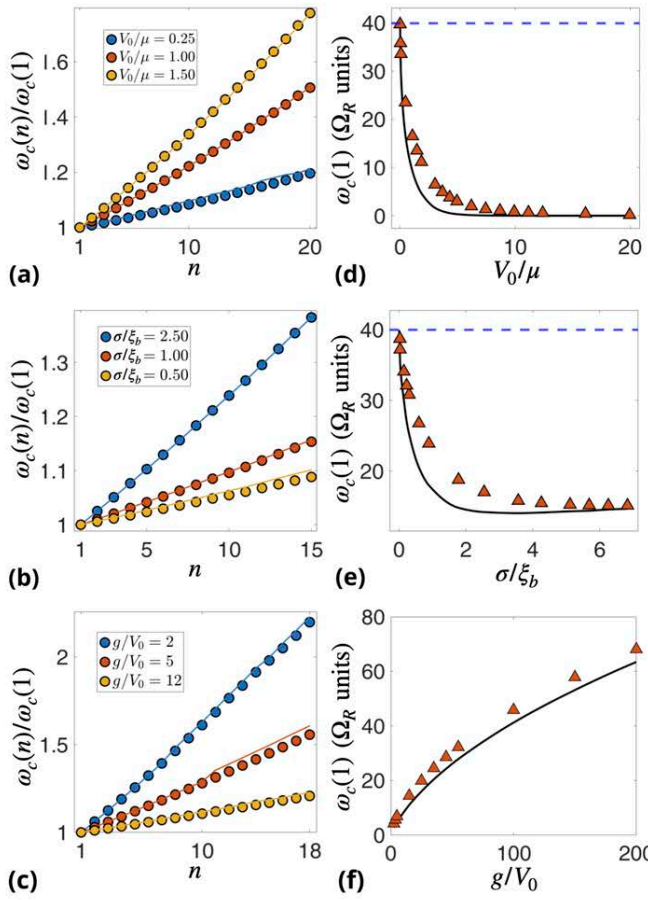


FIG. 3. Critical effective rotation frequency $\omega_c(n)$ as a function of the number of barriers n for different system's parameters. In panels 3(a)–(c), the critical frequency is normalized to its value at $n = 1$, i.e., $\omega_c(n)/\omega_c(1)$. We vary the barrier height V_0/μ in (a), the barrier width σ/ξ_b in (b), and the coupling constant g (reporting the ratio g/V_0) in (c). Dots show the numerical solutions of Eq. (8), while solid lines correspond to the prediction of Eq. (18). Panels 3(d)–(f) display the critical frequency at a single barrier, $\omega_c(1)$, as a function of V_0/μ (d), σ/ξ_b (e), and g/V_0 (orange triangles). The black solid line is Eq. (20). Parameters are: (a) $g = 5000$ and $\sigma/\xi_b \approx 1.2$; (b) $g = 10^4$ and $V_0/\mu \approx 0.7$; (c) $\sigma/\xi_b \approx 0.6$ and $V_0/\mu \approx 2.2$; (d) $g = 10^4$ and $\sigma/\xi_b \approx 0.9$; (e) $g = 10^4$ and $V_0/\mu \approx 0.12$; (f) $V_0/\mu \approx 0.12$ and $\sigma/\xi_b \approx 0.9$.

changing the circulation v and/or the rotation angular velocity Ω .

The behavior of ω_c as a function of n is shown in Fig. 2(d). The effective critical frequency increases monotonically with the number of barriers, n , as already suggested qualitatively by Fig. 2(c). This monotonic dependence shows that the system becomes progressively more resilient to dynamical instabilities as n increases, which is one of the main results of this work. For small n , when the density modulations associated with neighboring barriers do not significantly overlap, the dependence of ω_c on n is approximately linear, as clarified in the following section.

B. Increased stability with the number of barriers

The mechanism underlying the enhanced stabilization can be understood in terms of two basic principles: particle-number conservation, enforced by density normalization, and circulation quantization, imposed by Eq. (2). In general, the density profile $\rho(\theta)$ obtained from Eq. (8) depends on both the effective rotation frequency ω and the number of barriers n . We make this dependence explicit by writing $\rho(\theta, \omega, n)$. As shown in Fig. 1, under the condition of well-separated barriers, $\theta_{j+1} - \theta_j \gg \xi_b, \sigma$, the density profile consists of a uniform bulk density and a set of identical depleted regions localized at the barriers. Density normalization gives

$$\int_0^{2\pi} \rho(\theta, \omega, n) d\theta = \rho_b(\omega, n) [2\pi - 2\tilde{\sigma}n] + n \int_{-\tilde{\sigma}}^{+\tilde{\sigma}} \rho(\theta, \omega, n) d\theta = 1, \quad (13)$$

where $\tilde{\sigma}$ is the characteristic length over which the density rises from its minimum at the barrier to the bulk value $\rho_b(\omega, n)$. When $\xi_b \ll \sigma$, this length is on the order of the barrier half-width, $\tilde{\sigma} \approx \sigma$. Equation (13) leads to

$$\rho_b(\omega, n) = \frac{1}{2\pi} \frac{1 - n \int_{-\tilde{\sigma}}^{+\tilde{\sigma}} \rho(\theta, \omega, n) d\theta}{1 - n \tilde{\sigma}/\pi}. \quad (14)$$

The integral in Eq. (14) depends only weakly on n and, since the density is depleted in the interval $[-\tilde{\sigma}, \tilde{\sigma}]$, it is always smaller than $\tilde{\sigma}/\pi$. Equation (14) therefore predicts an increase of ρ_b with n .

Next, we analyze how increasing n affects the superfluid phase, $\phi(\theta)$, along the ring. Using the quantization of circulation, we introduce the phase jump across a single barrier as

$$\delta\phi(\omega, n) = \frac{1}{n} \int_0^{2\pi} [\nu(\theta, \omega, n) - \nu_b] d\theta, \quad (15)$$

where $\nu(\theta, \omega, n) = J/\rho(\theta, \omega, n) + \Omega$ is the superfluid velocity and $\nu_b = J/\rho_b + \Omega$ is its bulk value. Using Eq. (5), we obtain

$$\delta\phi(\omega, n) = \frac{2\pi\omega}{I(\omega, n)^{-1} + n}, \quad (16)$$

where

$$I(\omega, n) = \int_{-\tilde{\sigma}}^{+\tilde{\sigma}} \left(\frac{\rho_b(\omega, n)}{\rho(\theta, \omega, n)} - 1 \right) d\theta. \quad (17)$$

The integral in Eq. (17) encodes the relative density depletion inside the barrier, $[\rho_b(\omega, n) - \rho(\theta, \omega, n)]/\rho(\theta, \omega, n)$, and is expected to depend only weakly on n . Neglecting this dependence, Eq. (16) shows that $\delta\phi(\omega, n)$ decreases with increasing n at fixed ω [52]. A detailed numerical analysis (see Appendix) confirms this trend.

The instability sets in when the phase jump across each barrier reaches a critical value $\delta\phi_c$, beyond which phase slips are triggered. Since $\delta\phi(\omega, n)$ decreases with n at fixed ω , increasing the number of barriers moves the system away from the phase-slip threshold. This provides a qualitative explanation of the enhanced stability observed in Fig. 1(a) and Fig. 2(d).

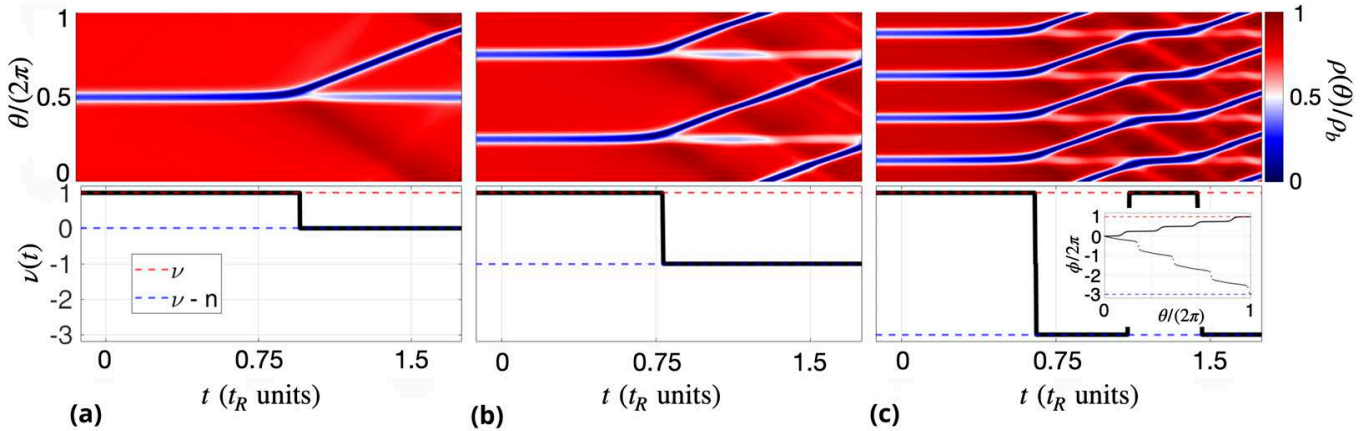


FIG. 4. Joint emission of solitons in the clean necklace. Each panel shows the time evolution of the density profile (top) and the winding number $\nu(t)$ (bottom). Different panels correspond to different numbers of barriers: $n = 1$ (a), $n = 2$ (b), and $n = 4$ (c). In each case, the rotation frequency is quenched to a value $\omega = \omega_c(n) + \delta\omega$, with $\delta\omega \approx 0.05$. In the lower panels, the red dashed line indicates the initial winding number $\nu(0) = 1$, while the blue dashed line marks the value $\nu = \nu(0) - n$ observed immediately after soliton emission. The inset in panel (c) shows the superfluid phase as a function of θ at different times: $t = 0.5$ (solid line), corresponding to a circulation $\nu = 1$, and $t = 1$ (dotted line), corresponding to a circulation $\nu = -3$. Parameters are the same as in Fig. 2.

Focusing now on the critical frequency, Eq. (16) gives

$$\omega_c(n) = \frac{\delta\phi_c(n)}{2\pi} \left(\frac{1}{I_c(n)} + n \right), \quad (18)$$

where $\delta\phi_c(n) \equiv \delta\phi(\omega = \omega_c, n)$ and $I_c(n) \equiv I(\omega = \omega_c, n)$ denote the values at the critical point. Equation (18) is a nonlinear implicit relation for $\omega_c(n)$. However, we find numerically that both $\delta\phi_c(n)$ and $I_c(n)$ vary only weakly with n (see Appendix). This implies that $\omega_c(n) \propto n$.

A further simplification holds in the Josephson (tunneling) regime, where $\delta\phi_c \approx \pi/2$. Neglecting again the dependence of $I_c(n)$ on n , we obtain

$$\omega_c(n) \approx \omega_0 + \frac{n}{4}, \quad (19)$$

with $\omega_0 = 1/(4I_c)$. Equation (19) predicts that the slope of $\omega_c(n)$ as a function of n is equal to $1/4$, independent of the other system's parameters. In Appendix, we compare this prediction with the numerical results and find an overall good agreement, with deviations due to the approximations discussed above.

In Fig. 3(a)–(c), we show the results of numerical simulations for $\omega_c(n)$ as a function of n (dots), obtained by varying the barrier height V_0 , the width σ , and the coupling constant g , respectively. Solid lines are the prediction of Eq. (18) [59]. The stabilization effect is present both in the weak-link ($V_0/\mu < 1$) and in the Josephson ($V_0/\mu > 1$) regimes. In particular, the slope of $\omega_c(n)$ increases with V_0/μ . We also explore a wide range of barrier widths, covering both the hydrodynamic regime ($\sigma/\xi_b > 1$) and the thin-barrier regime ($\sigma/\xi_b < 1$), and find that the slope of $\omega_c(n)$ increases with σ/ξ_b .

Overall, enhancing the barrier effect (e.g., by increasing V_0/μ or σ/ξ_b , or by decreasing g) increases the separation between the critical frequencies at successive n , thereby making

the stabilization mechanism more pronounced, i.e., yielding a larger slope of $\omega_c(n)$. Conversely, for very strong interactions (large g) or vanishingly weak and narrow barriers (small V_0/μ and σ/ξ_b), the stabilization effect is still observed, but with very weak increase of $\omega_c(n)$ with n . Overall, our analysis confirms that the enhancement of rotational stability is primarily controlled by the number of barriers, rather than by microscopic details of the potential.

In Fig. 3(a)–(c), $\omega_c(n)$ is normalized to the corresponding value at $n = 1$, $\omega_c(1)$. For completeness, Figs. 3(d)–(f) show $\omega_c(1)$ as a function of V_0/μ , σ/ξ_b , and g , respectively. Increasing V_0 (at fixed g and $\sigma/\xi_b \approx 1.3$) leads to a decrease of $\omega_c(1)$; a similar trend is observed when increasing σ at constant V_0 and g . In particular, in the limit $g \rightarrow 0$ we find that the slope of $\omega_c(n)$ as a function of n increases [panel (c)], while $\omega_c(1)$ tends to zero [panel (f)].

C. Comparison with the Landau instability criterion

As discussed above, the critical frequency ω_c marks the onset of a dynamical instability in the rotating system. It is therefore natural to compare our results with the Landau instability criterion, derived in Ref. [48] for a 1D superfluid with a single potential barrier. In that framework, the instability is expected when the superfluid velocity in the frame co-moving with the barrier, $J/\rho(\theta)$, equals the local sound speed $c_s(\theta) = \sqrt{g\rho(\theta)}$. This condition is first met at the barrier center (at $\theta = \theta_j$), where the density is minimal and the velocity is maximal, according to Eq. (4). Imposing $J/\rho_0 = \sqrt{g\rho_0}$, where ρ_0 is the density at the center of the barrier, gives

$$\omega_c = \frac{2\pi\sqrt{g\rho_0^3}}{f_s}. \quad (20)$$

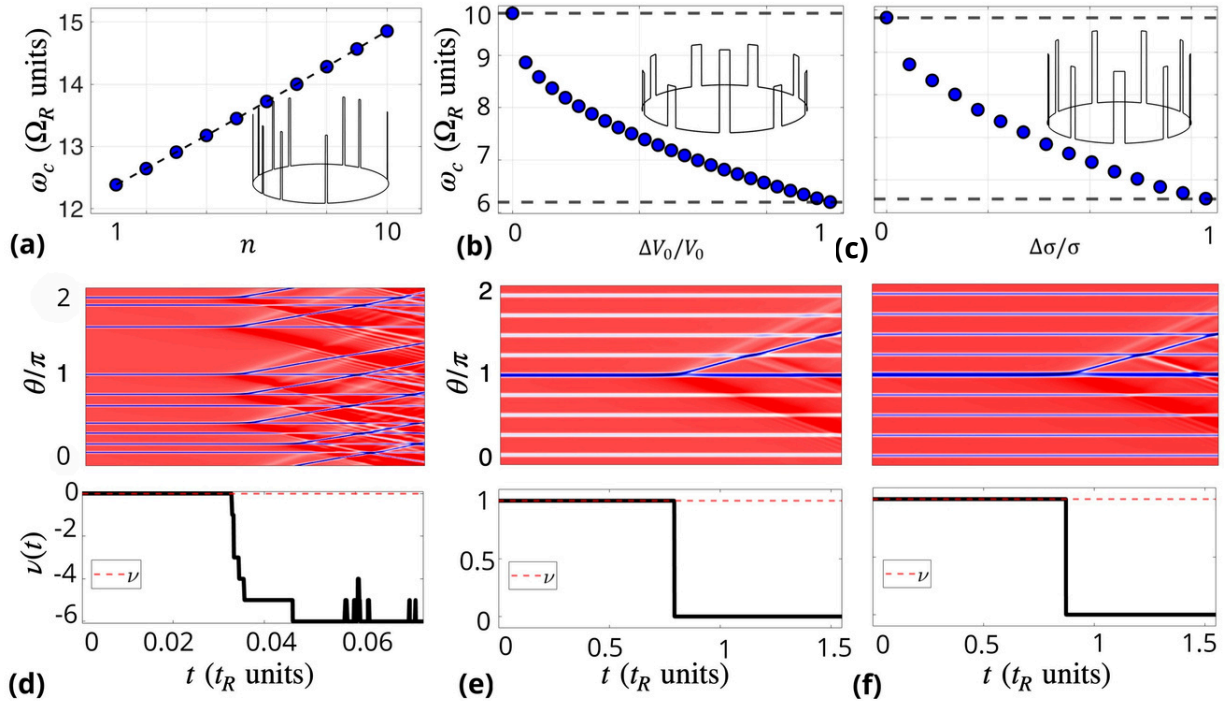


FIG. 5. Panels (a)–(c) show the critical frequency in the dirty necklace with non-uniform square barriers; examples of the corresponding potentials are displayed in the insets. Panels (d)–(f) present the associated density dynamics (top) and winding number (bottom) as a function of time. In all cases, the dynamics is triggered by quenching the rotation frequency to $\omega = \omega_c(n) + \delta\omega$, with $\delta\omega \simeq 0.05$. (a), (d): randomly distributed barriers (see inset). Panel (a) shows $\omega_c(n)$ (dots) as a function of n , obtained by averaging over 30 random realizations of the potential (the rms fluctuations are smaller than the symbol size). The dashed line corresponds to a uniform necklace with the same n , V_0 , and σ . Here, $g = 10^4$, $V_0/\mu \sim 1$, $\sigma/\xi \sim 1$, and $\nu(0) = 0$. (b), (e): non-uniform barrier height. One barrier has height V_0 , while the remaining $n-1$ barriers have height $V_0 - \Delta V$. Panel (b) shows the critical frequency as a function of $\Delta V_0/V_0$. (c), (f): non-uniform barrier width. One barrier has width σ , while the remaining $n-1$ barriers have width $\sigma - \Delta\sigma$. Panel (c) reports the critical frequency as a function of $\Delta\sigma/\sigma$. In panels (b) and (c), the upper dashed line indicates ω_c for n identical barriers, while the lower dashed line gives ω_c for a single barrier ($n = 1$). In panels (b), (c), (e), (f), the parameters are $n = 9$, $g = 5000$, $V_0/\mu \sim 0.6$, $\sigma/\xi_b \sim 6$, and $\nu(0) = 1$.

In Figs. 3(d)–(f) we compare the prediction of Eq. (20) (black solid lines) with the numerical data for a single barrier (orange triangles). Our results are consistent with previous theoretical studies [47, 48], which show that the critical velocity associated with a Landau instability decreases as the barrier strength is increased (either by raising the barrier height V_0 or its half-width σ). Conversely, when the barrier becomes weaker, the critical frequency approaches the bulk sound velocity $\sqrt{g\rho_b}$, as expected for a nearly uniform superfluid [47, 48]. Since the sound speed increases with g , stronger interactions enhance the robustness of the system against perturbations, leading to higher critical frequencies.

Equation (20), originally derived in the hydrodynamic regime [48], also agrees well with our simulations in the thin-barrier limit ($\sigma/\xi_b \ll 1$) and for weak barriers ($V_0/\mu < 1$). In the intermediate regime $\sigma \sim \xi_b$, however, Eq. (20) exhibits systematic deviations from the numerical data, although it reproduces the qualitative dependence on σ/ξ_b . In this case, the condition $J/\rho = c_s$ is not fulfilled exactly at the barrier center but rather within a distance of order ξ_b from it, so that the Landau critical velocity corresponds to a fraction of the bulk sound speed $\sqrt{g\rho_b}$, larger than the minimum value $\sqrt{g\rho_0}$.

D. Soliton emission and inversion of the current

We now explore the behavior of the system for $\omega > \omega_c$ – the regime indicated as “soliton-dominated” in Fig. 1(a). We perform real-time simulations of Eq. (1). The superfluid is initially prepared in the ground state in stable regime, with $\omega < \omega_c$. At time $t = 0$, the rotation frequency is quenched to a value $\omega + \Delta\omega > \omega_c$. Here we consider $\Delta\omega \ll \omega_c$ in order to limit spurious excitations.

After the quench, the system becomes dynamically unstable and, as suggested by the discussion in Sec. III A, it relaxes by emitting solitons. The ensuing dynamics is particularly rich: representative examples are shown in Fig. 4(a)–(c). In the upper panels, we plot the co-rotating density profile $\rho(\theta)$ for $n = 1, 2, 4$, respectively, as a function of time. Initially, the density exhibits a dip at the position of each barrier; in the co-rotating frame the barriers are at rest. After a time of the order of a fraction of $t_R = \hbar/(mR^2)$, we observe the simultaneous emission of n dark solitons, one from each barrier. Once formed, the solitons propagate along the ring, as visible from the slanted density dips. The density remains depleted at the barrier positions, and sound waves are emitted, propagating in the direction opposite to the soliton motion. As clearly visible

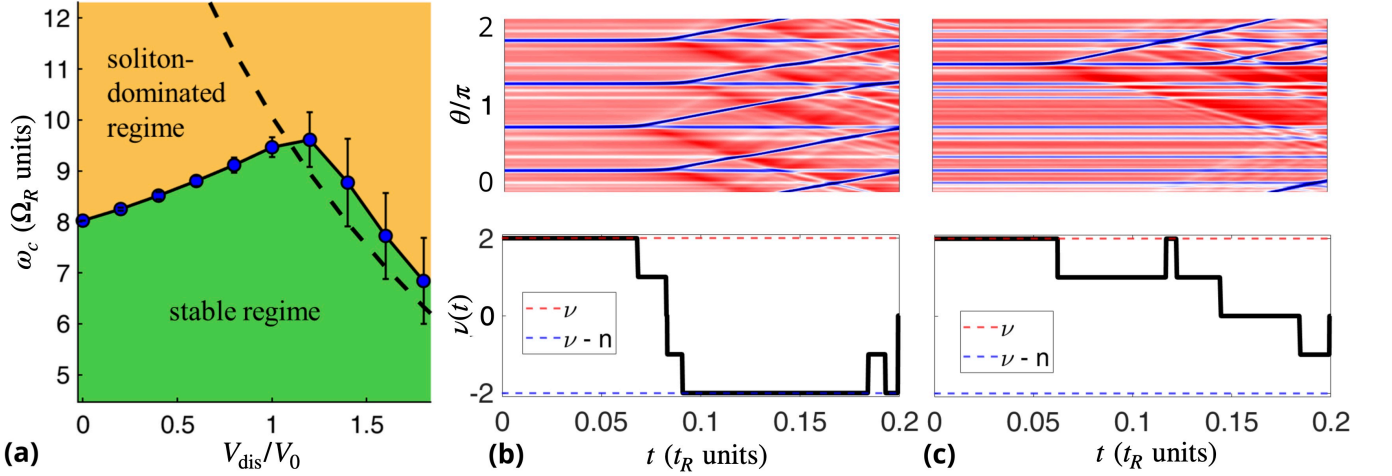


FIG. 6. (a) Critical frequency ω_c in the dirty necklace (blue dots), as a function of V_{dis}/V_0 and for $n = 4$. Data are obtained by averaging over 35 different realizations of the speckle potential, with error bars giving the standard deviation. The black line is a guide to the eye, while the black dashed line is ω_c for the sole speckle disorder. As in Fig. 1(b), the green (yellow) shading highlights the stable (unstable) region. Panels (b) and (c) show the density (top) and the corresponding winding number $\nu(t)$ (bottom) as a function of time for $V_{dis} = 0.6V_0$ and $V_{dis} = 1.4V_0$, respectively. The dynamics is triggered by a quench to $\omega = \omega_c + \delta\omega$, with $\delta\omega \approx 0.01$. Parameters are $g = 3000$, $V_0/\mu \sim 0.5$, $\sigma/\xi_b \sim 2$ and $\sigma/\gamma \sim 2$, where γ is the disordered potential's correlation length.

in panel (c), solitons may remain pinned to a barrier for some time before being re-emitted.

The lower panels of Fig. 4(a)–(c) show the circulation $\nu(t) = \phi(2\pi, t) - \phi(0, t)$ [see Eq. (2)] as a function of time. We observe sudden jumps in $\nu(t)$ when solitons are emitted from the barriers; the jump is quantized and equal to the number of emitted solitons. This phase slip process has been observed in similar regimes involving quantized vortices [37, 60, 61]. After the joint soliton emission, the winding number takes the value $\nu(t) = \nu(0) - n$ (dashed blue line), where $\nu(0)$ is the initial circulation (dashed red line, $\nu = 1$ in the figure) and n is the number of barriers. A particularly interesting scenario occurs for $\nu(0) = 1$ and $n = 2$ [Fig. 4(b)], where the winding number reaches $\nu(t) = -1$ for sufficiently long evolution times, effectively realizing a switch that reverses the circulation. For $\nu(0) = 1$ and $n = 4$ [Fig. 4(c)], soliton emission not only reverses the sign of the circulation but also drives it to $\nu(t) = -3$, i.e., below $-\nu(0)$. When solitons pass through the barrier region, they can be temporarily absorbed, during which interval the winding number returns to its initial value $\nu(0)$. In the inset of Fig. 4(c) we show the superfluid phase at time $t = 0.5$ (solid line), when the circulation is equal to $\nu(0)$, and at $t = 1$ (dotted line), when the circulation has dropped by a factor n .

Overall, these results demonstrate that, by tuning the number of barriers in the clean necklace, one can control the phase-slip dynamics and, consequently, the circulation in the ring.

IV. DIRTY NECKLACE

In the previous analysis all barriers were identical and equally spaced, characterized by the same height V_0 and width

σ . We now relax this condition and refer to the case of a non-uniform ring potential as *dirty necklace*.

A. Non-uniform square barrier potentials

We first consider the case

$$V(\theta) = \begin{cases} V_0^{(i)}, & \text{for } \theta \in [\theta_i - \sigma^{(i)}, \theta_i + \sigma^{(i)}], \\ 0, & \text{otherwise,} \end{cases} \quad (21)$$

where the superscript emphasizes that these parameters may differ from barrier to barrier. In Fig. 5(a) we plot $\omega_c(n)$ as a function of n (dots) for a configuration in which the barrier centers θ_i are randomly sampled under the constraint $\theta_{i+1} - \theta_i \geq 2\xi_b$ [see inset of Fig. 5(a)]. Otherwise, all barriers have the same height and width, $V_i = V_0$ and $\sigma_i = \sigma$. This condition guarantees the existence of regions with well-defined bulk density ρ_b , consistent with the discussion above. Although spatial periodicity is lost, the stabilization effect persists: the critical frequency ω_c still increases almost linearly with n , and the numerical data for random configurations essentially coincide with the uniform case (black dashed line). This robustness arises because, in this setting, the clean and dirty necklaces share the same phase drop at each barrier. In contrast, the soliton dynamics following a quench of ω differs from the periodic case, as shown in Fig. 5(d) for $n = 10$. Solitons are nucleated at different times, and within the simulated time window only a subset of the barriers emits a soliton. As a consequence, $\nu(t) \neq \nu(0) - n$, since the number of emitted solitons is smaller than n . Nevertheless, even in this situation it is possible to invert the circulation.

A different scenario arises when the barriers remain equally spaced but one of them differs in height or width from the oth-

ers. These cases are shown in Figs. 5(b) and (c), respectively. Specifically, we consider $n - 1$ barriers with modified parameters (height $V_0^{(i)} = V_0 - \Delta V$ or half-width $\sigma^{(i)} = \sigma - \Delta\sigma$), while keeping the j -th barrier unperturbed (height $V_0^{(j)} = V_0$, half-width $\sigma^{(j)} = \sigma$). We vary ΔV from 0 to V_0 and $\Delta\sigma$ from 0 to σ , so that the limiting case corresponds to a single-barrier configuration. The top dashed line in Figs. 5(b) and (c) shows the uniform case with $n = 9$ identical periodic barriers, while the bottom dashed line indicates the critical frequency for $n = 1$. Increasing $\Delta V/V_0$ or $\Delta\sigma/\sigma$ lowers $\omega_c(n)$ with respect to the clean necklace. The asymmetry distorts the otherwise uniform phase distribution and redistributes the total phase drop unevenly among the barriers. Importantly, the reduction of $\omega_c(n)$ is not abrupt: the system with n barriers remains more stable than the single-barrier case. The behavior is mainly governed by the overall properties of the barrier array, which determine how the phase drop $\delta\phi$ is shared across the ring. The corresponding soliton dynamics, shown in Figs. 5(e) and (f) for finite ΔV and $\Delta\sigma$, exhibits similar features to the non-periodic case. When the rotation frequency is quenched above ω_c , we typically observe the emission of a single soliton. The associated phase slip changes $v(t)$ by ± 1 , adding or removing one quantum of circulation. The soliton nucleates at the strongest barrier (largest $V_0^{(i)}$ or $\sigma^{(i)}$), where the density depletion is maximal.

Overall, these results indicate that the stabilization induced by $n - 1$ barriers, compared to the single-barrier case, does not rely on perfect periodicity. This motivates the study of a fully disordered configuration, where the n -barrier necklace is superimposed on a non-uniform background potential, as discussed in the next section.

B. Combination of squared barriers and speckle disorder

We finally consider the case of a random disordered potential added to the clean necklace of Eq. (9):

$$V(\theta) = \begin{cases} V_0, & \text{for } \theta \in [\theta_j - \sigma, \theta_j + \sigma], \\ V_{\text{sp}}(\theta), & \text{elsewhere,} \end{cases} \quad (22)$$

where $\theta_j = 2\pi j/n$ and $V_{\text{sp}}(\theta)$ is a disordered speckle potential [62–65] of maximum height V_{dis} and correlation length γ .

In Fig. 6(a) we show the critical frequency $\omega_c(n)$ as a function of the disorder amplitude V_{dis} for $n = 4$. Each point is obtained by averaging over 30 independent realizations of the speckle potential. We find that ω_c increases with V_{dis} and reaches a maximum around $V_{\text{dis}} \sim V_0$. For stronger disorder, $V_{\text{dis}} \gtrsim V_0$, the speckle potential dominates over the periodic barriers: the critical frequency decreases mainly due to the peaks of the disordered potential having random height. The maximum of ω_c depends on the disorder correlation length γ : for lower σ/γ ratios (more correlated disorder) it shifts to smaller V_{dis} , whereas for very short correlation lengths ($\sigma/\gamma \gg 1$) ω_c may continue to increase even for $V_{\text{dis}} > V_0$. Overall, regardless of the specific parameters, we consistently observe an initial increase of ω_c with V_{dis} , as sketched in

Fig. 1(b): surprisingly, disorder enhances the stability of the system against dynamical excitations.

Figures 6(b) and (c) display the density profiles (top panels) and the winding number (bottom) as a function of time following a quench of ω . The dynamics is intermediate between the cases discussed above. When $V_{\text{dis}} \ll V_0$ [Fig. 6(b)], n solitons are emitted, as in Fig. 3, although their emission is not strictly simultaneous. The winding number decreases in steps of n , so that $v(t) = v(0) - n$ after emission. In contrast, when $V_{\text{dis}} \gtrsim V_0$ [Fig. 6(c)], solitons are emitted only from the strongest effective barriers, corresponding to the deepest density minima, as in Figs. 5(e) and (f). In this regime, $v(t)$ changes by one unit at a time, for each emitted soliton.

V. CONCLUSIONS

Our work, focused on a 1D BEC at zero temperature, has allowed us to systematically explore a wide range of parameters and to obtain analytical results regarding the enhanced robustness of the superfluid necklace to dynamical excitations. Despite its simplicity, the model captures effects that are expected to persist in more complex systems and geometries. In particular, we have shown that the stabilization mechanism induced by multiple barriers is present in both the hydrodynamic and tunneling regimes, with the slope of the critical effective rotation frequency $\omega_c(n)$ increasing with the barrier height and width. Moreover, we have unveiled a rich dynamics in the unstable regime: in the clean ring, solitons are emitted simultaneously from each barrier, enabling counterintuitive configurations in which the circulation can be controlled and even reversed by tuning ω and the number of barriers. The stabilization effect has a robust topological nature that extends to dirty necklaces with imperfections and inhomogeneities. Remarkably, a disordered potential of moderate amplitude can further enhance $\omega_c(n)$, offering a novel perspective on the subtle and counterintuitive interplay between superflow and impurities [66–69]. Beyond motivating new experimental investigations, our results call for advanced theoretical studies and extensions to Fermi superfluids [70] and supersolids [71–74] in toroidal traps, as well as for the inclusion of thermal and quantum fluctuations [75–78]. In summary, our work demonstrates the possibility of exploiting multiply connected geometries to engineer both stable and unstable dynamics in ring superfluids over a broad range of parameters, with direct relevance for current experiments and atomtronic devices [79–81].

VI. ACKNOWLEDGMENTS

We thank Marzena Ciszak, Giulia Del Pace, Beatrice Donelli, Nicola Grani, Diego Hernandez-Rajkov, Francesco Marino, Giacomo Roati, Francesco Scazza and Klejdja Xhani for discussions. This work has been supported by the Horizon Europe programme HORIZON-CL4-2022-QUANTUM-02-SGA (project PASQuanS2.1, GA no. 101113690).

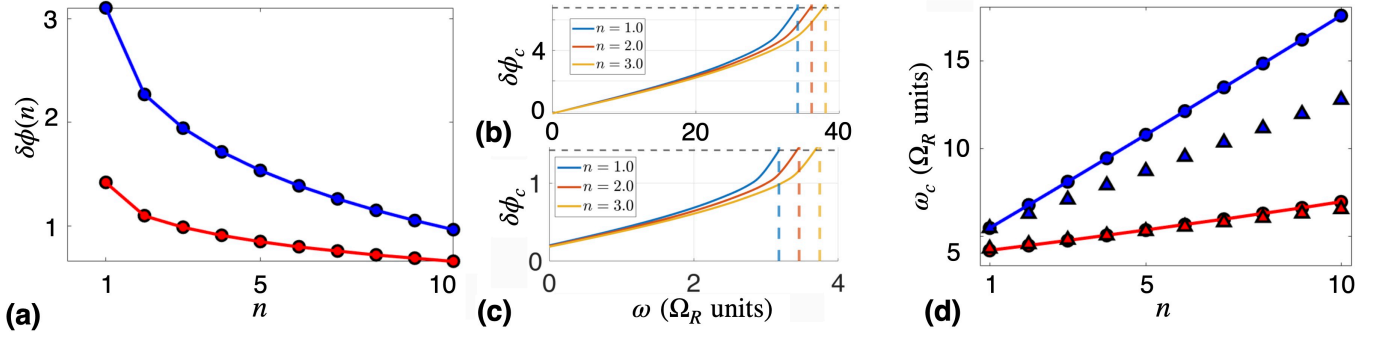


FIG. 7. (a) Phase jump $\delta\phi$ as a function of the number of obstacles n . Red (Blue) data reports the Josephson (hydrodynamic) results. Full dots represent numerical results, while solid lines report the prediction of Eq. (16). Panels (b) and (c) report the phase jump $\delta\phi$ as a function of the rotation frequency ω , for different barrier number (see legend). Panels (b) reports the result in the hydrodynamic regime, while panel (c) reports the Josephson regime data. Vertical dashed lines highlight the values of $\delta\phi_c$ for different n , while dashed horizontal line reports the value of $\delta\phi_c(1)$. (d) Critical frequency ω_c as a function of the number of barriers n . Red (Blue) data reports the Josephson (hydrodynamic) results. Dashed lines report numerical results. Circles show numerical results, while solid lines report the prediction of Eq. (18). Blue triangles report Eq. (18) for fixed values of $I_c(n)$ and $\delta\phi_c$ (to the $n=1$ value). Red triangles reports the prediction of Eq. (19), valid in the Josephson regime. Parameters are $g = 10^4$, $V_0/\mu \sim 1.8$, $\sigma/\xi_b \sim 0.9$ in the Josephson regime and $g = 10^5$, $V_0/\mu \sim 0.4$ and $\sigma/\xi_b \sim 28$ in the hydrodynamic regime.

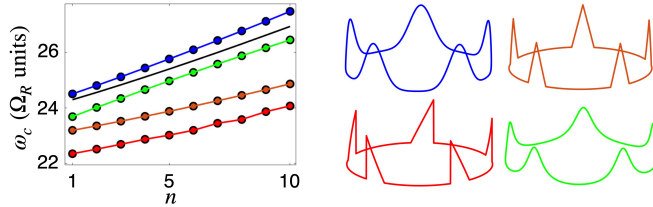


FIG. 8. The left panel reports Critical frequency ω_c as a function of n for barriers having different shapes: Gaussian (blue), triangular (orange), tilted triangular (red), Lorentzian (green). The corresponding potential $V(\theta)$ is shown on the right side, for the case $n = 5$. Lines crossing the points are guide to the eye. The solid black line is the case of squared barriers. Data for different colors are shifted vertically for better visibility. Parameters are $g = 5000$, $V_0/\mu \sim 0.25$, $\sigma/\xi_b \sim 6$, where σ is the effective barrier half-width (Gaussian standard deviation, Lorentzian half-width, and half the triangular base).

VII. APPENDIX

A. Phase jump and instability

As discussed in Sec. (III B), the increase of the critical frequency $\omega_c(n)$ with n is associated to the redistribution of the phase drop $\delta\phi(\omega, n)$ across each potential barrier. Here, we provide a numerical analysis of Eqs. (15) and (16), both in the hydrodynamic and Josephson regimes, and show that the critical value $\delta\phi_c = \delta\phi(\omega_c)$ depends only weakly on n . Figure (7)(a) reports the prediction of Eq. (16) for two different transport regimes; hydrodynamic ($V_0/\mu \ll 1$, $\sigma \gg \xi_b$, $\tilde{\sigma} \sim 3\sigma$, blue line) and Josephson ($V_0/\mu > 1$, $\sigma \sim \xi_b$, $\tilde{\sigma} \sim 6\xi_b$, red line). Dots represent numerical data, given by Eq. (15). The phase jump $\delta\phi$ is observed to decrease for increasing n and fixed Ω , in agreement with Eq. (15). Figure (7)(b) and (7)(c) report the values of $\delta\phi(\Omega, n)$ as a function of Ω for the regimes of Fig. (7)(a) and for $n = 1, 2, 3$.

Horizontal dashed line reports the value of $\delta\phi_c(1)$. Vertical colored lines mark the different values of ω_c for $n = 1, 2, 3$. We find that $\delta\phi(\Omega, n)$ increases with Ω at fixed n . Moreover, the critical value $\delta\phi_c = \delta\phi(\omega_c)$ is approximately constant with n , increasing only weakly. This supports the conclusion of Sec. (III B): increasing n enhances stability because it reduces the phase jump per barrier, $\delta\phi$. If $\delta\phi_c$ decreased with n as well, this argument would no longer hold, since the system would not be pushed further from the phase-slip threshold. Figure (7)(d) reports the critical frequency ω_c as a function of n , for both the hydrodynamic (blue) and Josephson (red) regimes. Solid lines are Eq. (18) with $\tilde{\sigma} \sim 3\sigma$ (hydrodynamic) and $\tilde{\sigma} \sim 6\xi_b$ (Josephson). Dots are numerical results. Blue triangles are Eq. (18) with $\delta\phi_c(n) = \delta\phi_c(1)$ and $I_c(n) = I_c(1)$. Red triangles are Eq. (19), obtained for the Josephson regime. As we pointed out in Sec. (III B), keeping $\delta\phi_c$ and I_c fixed to their $n = 1$ value still predicts a linear behavior. Inclusion of the full dependence results in the solid blue line, which is fully compatible with numerical data. On the other hand, the prediction of Eq. (19) is approximately consistent with the numerical result, giving the correct order of magnitude but the incorrect slope. This discrepancy arises because $\delta\phi_c$ increases slightly with n at the critical point; as a result, Eq. (19) predicts an incorrect slope and appears as a secant line, crossing the numerical curve

B. Independency of the stabilization effect from the barrier shape

Throughout this manuscript we have focused on square barriers in order to exploit analytical solutions of Eq. (8). In this section we show that our main conclusions are qualitatively insensitive to the barrier shape. Figure 8 shows the critical frequency ω_c calculated for different barrier shapes: gaussian (blue), Lorentzian (green), triangular (orange), "grid-

like”(red). Black solid line is the critical frequency calculated for a square-barrier potential as Fig. 1(a). Despite the different barriers’ shape, we observe the same qualitative behavior as in the main paper: a linear increase with n as long as nearby

barriers are well-separated (i.e. $\theta_i - \theta_{i-1} > 2\xi_b, \sigma$). This supports our claim that the stability of the system increases due to a redistribution of the phase jump $\delta\phi$ across the barriers when increasing n .

[1] L. Landau, Theory of the superfluidity of helium II, *Phys. Rev.* **60**, 356–358 (1941).

[2] A. J. Leggett, Bose-Einstein condensation in the alkali gases: Some fundamental concepts, *Rev. Mod. Phys.* **73**, 307 (2001).

[3] C. J. Pethick and H. Smith, *Bose-Einstein Condensation in Dilute Gases*, 2nd ed. (Cambridge University Press, Cambridge, 2008).

[4] A. G. Sykes, M. J. Davis, and D. C. Roberts, Drag force on an impurity below the superfluid critical velocity in a quasi-one-dimensional Bose-Einstein condensate, *Phys. Rev. Lett.* **103**, 085302 (2009).

[5] B. Wu and Q. Niu, Landau and dynamical instabilities of the superflow of Bose-Einstein condensates in optical lattices, *Phys. Rev. A* **64**, 061603(R) (2001).

[6] G. E. Astrakharchik and L. P. Pitaevskii, Motion of a heavy impurity through a Bose-Einstein condensate, *Phys. Rev. A* **70**, 013608 (2004).

[7] F. Pinsker, Gaussian impurity moving through a Bose-Einstein superfluid, *Physica B* **521**, 36 (2017).

[8] C. Raman, M. Köhl, R. Onofrio, D. S. Durfee, C. E. Kuklewicz, Z. Hadzibabic, and W. Ketterle, Evidence for a Critical Velocity in a Bose-Einstein Condensed Gas, *Phys. Rev. Lett.* **83**, 2502 (1999).

[9] R. Onofrio, C. Raman, J. M. Vogels, J. R. Abo-Shaeer, A. P. Chikkatur, and W. Ketterle, Observation of Superfluid Flow in a Bose-Einstein Condensed Gas, *Phys. Rev. Lett.* **85**, 2228 (2000).

[10] M. W. Zwierlein, J. R. Abo-Shaeer, A. Schirotzek, C. H. Schunck, and W. Ketterle, Vortices and superfluidity in a strongly interacting Fermi gas, *Nature* **435**, 1047–1051 (2005).

[11] M. R. Matthews, B. P. Anderson, P. C. Haljan, D. S. Hall, C. E. Wieman, and E. A. Cornell, “Vortices in a Bose-Einstein Condensate,” *Phys. Rev. Lett.* **83**, 2498–2501 (1999).

[12] F. S. Cataliotti, S. Burger, C. Fort, P. Maddaloni, F. Minardi, A. Trombettoni, A. Smerzi, and M. Inguscio, Josephson junction arrays with Bose-Einstein condensates, *Science* **293**, 843 (2001).

[13] J. Kinast, S. L. Hemmer, M. E. Gehm, A. Turlapov, and J. E. Thomas, “Evidence for Superfluidity in a Resonantly Interacting Fermi Gas,” *Phys. Rev. Lett.* **92**, 150402 (2004).

[14] A. J. Leggett, Can a Solid Be “Superfluid”? *Phys. Rev. Lett.* **25**, 1543–1546 (1970).

[15] A. J. Leggett, On the superfluid fraction of an arbitrary many-body system at $T = 0$, *J. Stat. Phys.* **93**, 927–941 (1998).

[16] G. Chauveau, C. Maury, F. Rabec, C. Heintze, G. Brochier, S. Nascimbène, J. Dalibard, J. Beugnon, S. M. Roccuzzo, and S. Stringari, Superfluid fraction in an interacting spatially modulated Bose-Einstein condensate, *Phys. Rev. Lett.* **130**, 226003 (2023).

[17] G. Biagioni, N. Antolini, B. Donelli, L. Pezzè, A. Smerzi, M. Fattori, A. Fioretti, Carlo Gabbanini, Massimo Inguscio, Luca Tanzi, G. Modugno, Measurement of the superfluid fraction of a supersolid by Josephson effect, *Nature* **629**, 773 (2024).

[18] O. Morsch, J. H. Müller, M. Cristiani, D. Ciampini, and E. Arimondo, Bloch Oscillations and Mean-Field Effects of Bose-Einstein Condensates in 1D Optical Lattices, *Phys. Rev. Lett.* **87**, 140402 (2001).

[19] L. Fallani, L. De Sarlo, J. E. Lye, M. Modugno, R. Saers, C. Fort, and M. Inguscio, Observation of Dynamical Instability for a Bose-Einstein Condensate in a Moving 1D Optical Lattice, *Phys. Rev. Lett.* **93**, 140406 (2004).

[20] J. E. Lye, L. Fallani, M. Modugno, D. S. Wiersma, C. Fort, and M. Inguscio, Bose-Einstein Condensate in a Random Potential, *Phys. Rev. Lett.* **95**, 070401 (2005).

[21] D. Clément, A. F. Varón, M. Hugbart, J. A. Retter, P. Bouyer, L. Sanchez-Palencia, D. M. Gangardt, G. V. Shlyapnikov, and A. Aspect, Suppression of Transport of an Interacting Elongated Bose-Einstein Condensate in a Random Potential, *Phys. Rev. Lett.* **95**, 170409 (2005).

[22] M. Pasienski, D. McKay, M. White, and B. DeMarco, A disordered insulator in an optical lattice, *Nat. Phys.* **6**, 677–680 (2010).

[23] R. Desbuquois, L. Chomaz, T. Yefsah, J. Léonard, J. Beugnon, C. Weitenberg, and J. Dalibard, Superfluid behaviour of a two-dimensional Bose gas, *Nat. Phys.* **8**, 645 (2012).

[24] W. J. Kwon, G. Moon, S. W. Seo, and Y. Shin, Critical velocity for vortex shedding in a Bose-Einstein condensate *Phys. Rev. A* **91**, 053615 (2015).

[25] W. J. Kwon, J. H. Kim, S. W. Seo, and Y. Shin, Observation of von Kármán Vortex Street in an Atomic Superfluid Gas, *Phys. Rev. Lett.* **117**, 245301 (2016).

[26] S. Gupta, K. W. Murch, K. L. Moore, T. P. Purdy, and D. M. Stamper-Kurn, Bose-Einstein Condensation in a Circular Waveguide, *Phys. Rev. Lett.* **95**, 143201 (2005).

[27] C. Ryu, M. F. Andersen, P. Cladé, V. Natarajan, K. Helmerson, and W. D. Phillips, Observation of persistent flow of a Bose-Einstein condensate in a toroidal trap, *Phys. Rev. Lett.* **99**, 260401 (2007).

[28] A. Tononi and L. Salasnich, Low-dimensional quantum gases in curved geometries, *Nature Reviews Physics* **5**, 398 (2023).

[29] S. Moulder, S. Beattie, R. P. Smith, N. Tammuz, and Z. Hadzibabic, Quantized supercurrent decay in an annular Bose-Einstein condensate, *Phys. Rev. A* **86**, 013629 (2012).

[30] L. Corman, L. Chomaz, T. Bienaimé, R. Desbuquois, C. Weitenberg, S. Nascimbène, J. Dalibard, and J. Beugnon, Quench-induced supercurrents in an annular Bose gas, *Phys. Rev. Lett.* **113**, 135302 (2014).

[31] G. Del Pace *et al.*, Imprinting persistent currents in tunable fermionic rings, *Phys. Rev. X* **12**, 041037 (2022).

[32] Y. Cai, D. G. Allman, P. Sabharwal, and K. C. Wright, “Persistent Currents in Rings of Ultracold Fermionic Atoms,” *Phys. Rev. Lett.* **128**, 150401 (2022).

[33] S. Eckel *et al.*, Hysteresis in a quantized superfluid “atomtronic” circuit, *Nature* **506**, 200–203 (2014).

[34] S. Eckel, F. Jendrzejewski, A. Kumar, C. J. Lobb, and G. K. Campbell, Interferometric measurement of the current-phase relationship of a superfluid weak link, *Phys. Rev. X* **4**, 031052 (2014).

[35] F. Piazza, L. A. Collins, and A. Smerzi, Vortex-induced phase-slip dissipation in a toroidal Bose-Einstein condensate flowing

through a barrier, *Phys. Rev. A* **80**, 021601 (2009).

[36] A. Ramanathan *et al.*, Superflow in a toroidal Bose–Einstein condensate: An atom circuit with a tunable weak link, *Phys. Rev. Lett.* **106**, 130401 (2011).

[37] K. C. Wright, R. B. Blakestad, C. J. Lobb, W. D. Phillips, and G. K. Campbell, Driving phase slips in a superfluid atom circuit with a rotating weak link, *Phys. Rev. Lett.* **110**, 025302 (2013).

[38] K. C. Wright, R. B. Blakestad, C. J. Lobb, W. D. Phillips, and G. K. Campbell, Threshold for creating excitations in a stirred superfluid ring, *Phys. Rev. A* **88**, 063633 (2013).

[39] J. Polo, R. Dubessy, P. Pedri, H. Perrin, and A. Minguzzi, Oscillations and decay of superfluid currents in a one-dimensional Bose gas on a ring, *Phys. Rev. Lett.* **123**, 195301 (2019).

[40] K. Xhani, G. Del Pace, F. Scazza, and G. Roati, Decay of persistent currents in annular atomic superfluids, *Atoms* **11**, 109 (2023).

[41] T. Frisch, Y. Pomeau, and S. Rica, Transition to dissipation in a model of superflow, *Phys. Rev. Lett.* **69**, 1644–1647 (1992).

[42] T. A. Bell, J. A. P. Glidden, L. Humbert, M. W. J. Bromley, S. A. Haine, M. J. Davis, T. W. Neely, M. A. Baker, and H. Rubinsztein-Dunlop, Bose–Einstein condensation in large time-averaged optical ring potentials, *New J. Phys.* **18**, 035003 (2016).

[43] F. Jendrzejewski, S. Eckel, N. Murray, C. Lanier, M. Edwards, C. J. Lobb, and G. K. Campbell, “Resistive Flow in a Weakly Interacting Bose-Einstein Condensate,” *Phys. Rev. Lett.* **113**, 045305 (2014).

[44] T. W. Neely, E. C. Samson, A. S. Bradley, M. J. Davis, and B. P. Anderson, “Observation of Vortex Dipoles in an Oblate Bose-Einstein Condensate,” *Phys. Rev. Lett.* **104**, 160401 (2010).

[45] J. Denschlag, J. E. Simsarian, D. L. Feder, C. W. Clark, L. A. Collins, J. Cubizolles, L. Deng, E. W. Hagley, K. Helmerson, W. P. Reinhardt, S. L. Rolston, B. I. Schneider, and W. D. Phillips, “Generating Solitons by Phase Engineering of a Bose-Einstein Condensate,” *Science* **287**, 97–101 (2000).

[46] A. M. Kamchatnov and S. V. Korneev, “Stabilization of Solitons Generated by a Supersonic Flow of a Bose-Einstein Condensate Past an Obstacle,” *Phys. Rev. Lett.* **100**, 160402 (2008).

[47] V. Hakim, Nonlinear Schrödinger flow past an obstacle in one dimension, *Phys. Rev. E* **55**, 2835–2845 (1997).

[48] G. Watanabe, F. Dalfovo, F. Piazza, L. P. Pitaevskii, and S. Stringari, Critical velocity of superfluid flow through single-barrier and periodic potentials, *Phys. Rev. A* **80**, 053602 (2009).

[49] F. Kh. Abdullaev, R. M. Galimzyanov, and Kh. N. Ismatullaev, Quasi-1D Bose–Einstein condensate flow past a nonlinear barrier, *Phys. Lett. A* **376**, 3372–3376 (2012).

[50] C. Ryu, P. W. Blackburn, A. A. Blinova, and M. G. Boshier, Experimental realization of Josephson junctions for an atom SQUID, *Phys. Rev. Lett.* **111**, 205301 (2013).

[51] C. Ryu, E. C. Samson, and M. G. Boshier, Quantum interference of currents in an atomtronic SQUID, *Nat. Commun.* **11**, 3338 (2020).

[52] L. Pezzè, K. Xhani, C. Daix, N. Grani, B. Donelli, F. Scazza, D. Hernandez-Rajkov, W. J. Kwon, G. Del Pace, and Giacomo Roati, Stabilizing persistent currents in an atomtronic Josephson junction necklace, *Nat. Commun.* **15**, 4831 (2024).

[53] K. Xhani, G. Del Pace, N. Grani, D. Hernández-Rajkov, B. Donelli, G. Roati, and L. Pezzè, Tuning the critical current in toroidal superfluids via controllable impurities, *arXiv:2501.12345* (2025).

[54] A. Baratoff, J. A. Blackburn, and B. B. Schwartz, Current-phase relationship in short superconducting weak links, *Phys. Rev. Lett.* **25**, 1738 (1970).

[55] F. Piazza, L. A. Collins, and A. Smerzi, Current-phase relation of a Bose–Einstein condensate flowing through a weak link, *Phys. Rev. A* **81**, 033613 (2010).

[56] the coefficients entering Eqs. (10) and (11) are:

$$\Delta = \left(\rho_0 - \frac{2(\mu_0 - V_0)}{g} \right)^2 - \frac{4J^2}{g\rho_0}$$

$$\rho_1 = \frac{3}{2}\rho_0 - \frac{\mu_0 - V_0}{g} - \frac{\sqrt{\Delta}}{2}$$

$$\alpha_1^2 = g(\sqrt{\Delta} + \rho_1)$$

$$m_1 = \frac{\sqrt{\Delta}}{\sqrt{\Delta} + \rho_1}$$

$$\rho_2 = \sqrt{2}(\rho_0^2 - \rho_0 \frac{\mu_0 - V_0}{g} + \frac{J^2}{2g\rho_0})^{1/2}$$

$$\alpha_2^2 = 4g\rho_2$$

$$m_2 = \frac{\rho_2 - \rho_1 - \frac{\sqrt{\Delta}}{2}}{2\rho_2}$$

$$c_b = \rho_b - \frac{2\xi_b^2 J^2}{g\rho_b}$$

$$\phi_0 = \operatorname{arctanh}(\sqrt{(\rho_\sigma - 2\xi_b^2 J^2 / \rho_b) / c_b})$$

$$\rho_\sigma = \frac{g}{2V_0} \left(\rho_0^2 - \rho_b^2 + \frac{2\mu_0\rho_b}{g} - \frac{(\mu_0 - V_0)\rho_0}{g} + \frac{J^2}{g} (\rho_b^{-1} - \rho_0^{-1}) \right).$$

[57] A. Muñoz Mateo, A. Gallemí, M. Guilleumas, and R. Mayol, Persistent currents supported by solitary waves in toroidal Bose-Einstein condensates, *Phys. Rev. A* **91**, 063625 (2015).

[58] M. Syafwan *et al.*, Superfluid flow past an obstacle in annular Bose–Einstein condensates, *J. Phys. B: At. Mol. Opt. Phys.* **49**, 235301 (2016).

[59] In all cases, $\tilde{\sigma}$ is chosen sufficiently large to cover the region where the density is depleted, i.e., $\tilde{\sigma} \sim 3\text{--}10\xi_b$.

[60] K. Xhani *et al.*, Critical transport and vortex dynamics in a thin atomic Josephson junction, *Phys. Rev. Lett.* **124**, 045301 (2020).

[61] F. Piazza, L. A. Collins, and A. Smerzi, Vortex-induced phase-slip dissipation in a toroidal Bose–Einstein condensate flowing through a barrier, *Phys. Rev. A* **80**, 021601(R) (2009).

[62] L. Sanchez-Palencia, D. Clément, P. Lugan, P. Bouyer, G. V. Shlyapnikov, and A. Aspect, Anderson Localization of Expanding Bose-Einstein Condensates in Random Potentials, *Phys. Rev. Lett.* **98**, 210401 (2007).

[63] J. Billy, et al., Direct observation of Anderson localization of matter waves in a controlled disorder, *Nature* **453**, 891 (2007).

[64] L. Pezzè, and L. Sanchez-Palencia, Localized and extended states in a disordered trap *Phys. Rev. Lett.* **106**, 040601 (2011).

[65] The speckle is generated on the discrete grid $\theta_j = 2\pi j/N$ by Fourier filtering a complex random field with a top-hat aperture in momentum space. Its intensity $I(\theta_j) = |\psi(\theta_j)|^2$ is shifted to be non-negative and re-normalized such that its maximum value is unity.

[66] V. Neverov, Correlated disorder as a way towards robust superconductivity, *Commun. Phys.* **5**, 177 (2022).

[67] M. N. Gastiasoro and B. M. Andersen, Enhancing superconductivity by disorder, *Phys. Rev. B* **98**, 184510 (2018).

[68] M. Leroux, V. Mishra, J. P. C. Ruff, H. Claus, M. P. Smylie, C. Opagiste, P. Rodie‘re, A. Kayani, G. D. Gu, J. M. Tran- quada, W.-K. Kwok, Z. Islam, and U. Welp, Disorder raises the critical temperature of a cuprate superconductor, *Proc. Natl. Acad. Sci. USA* **116**, 10691 (2019).

[69] W.-K. Kwok, U. Welp, A. Glatz, A. E. Koshelev, K. J. Kihlstrom, and G. W. Crabtree, Vortices in high-performance high-temperature superconductors, *Rep. Prog. Phys.* **79**, 116501 (2016).

[70] B. Tüzemen, A. Barresi, G. Włazłowski, P. Magierski, and K. Xhani, Pair-breaking as the fundamental limit to persistent-current stabilization in fermionic superfluids, arXiv:2510.24309.

[71] M. N. Tengstrand, D. Boholm, R. Sachdeva, J. Bengtsson, and S. M. Reimann, Persistent currents in toroidal dipolar supersolids, *Phys. Rev. A* **103**, 013313 (2021).

[72] M. Sindik, T. Zawislak, A. Recati, and S. Stringari, Sound, superfluidity, and layer compressibility in a ring dipolar supersolid, *Phys. Rev. Lett.* **132**, 146001 (2024).

[73] B. Donelli, N. Antolini, G. Biagioni, M. Fattori, A. Fioretti, C. Gabbanini, M. Inguscio, L. Tanzi, G. Modugno, A. Smerzi, and L. Pezzè, Self-induced Josephson oscillations and self-trapping in a supersolid dipolar quantum gas, *Phys. Rev. A* **112**, L051302 (2025).

[74] N. Preti, N. Antolini, C. Drevon, P. Lombardi, A. Fioretti, C. Gabbanini, G. Ferioli, G. Modugno, and G. Biagioni, Single-fluid model for rotating annular supersolids and its experimental implications, arXiv:2510.26753.

[75] L. Amico, A. Osterloh, and F. S. Cataliotti, Quantum many particle systems in ring-shaped optical lattices, *Phys. Rev. Lett.* **95**, 063201 (2005).

[76] K. Snizhko, K. Isaieva, Y. Kuriatnikov, Y. Bidasyuk, S. Vilchinskii, and A. Yakimenko, Stochastic phase slips in toroidal Bose-Einstein condensates, *Phys. Rev. A* **94**, 063642 (2016).

[77] A. Kumar, S. Eckel, F. Jendrzejewski, and G. K. Campbell, Temperature-induced decay of persistent currents in a superfluid ultracold gas, *Phys. Rev. A* **95**, 021602(R) (2017).

[78] Z. Mehdi, A. S. Bradley, J. J. Hope, and S. S. Szigeti, Superflow decay in a toroidal Bose gas: the effect of quantum and thermal fluctuations, *SciPost Phys.* **11**, 080 (2021).

[79] B. T. Seaman, M. Krämer, D. Z. Anderson, and M. J. Holland, Atomtronics: Ultracold-atom analogs of electronic devices, *Phys. Rev. A* **75**, 023615 (2007).

[80] L. Amico, D. Anderson, M. Boshier, J. P. Brantut, L. C. Kwek, A. Minguzzi, and W. von Klitzing, Atomtronic circuits: From many-body physics to quantum technologies, *Rev. Mod. Phys.* **94**, 041001 (2022).

[81] J. Polo, W. J. Chetcuti, E. C. Domanti, P. Kitson, A. Osterloh, F. Perciavalle, V. Pal Singh, L. Amico, Perspective on new implementations of atomtronic circuits, *Quantum Science and Technology* **9**, 030501 (2024).